All-or-none disconnection of pyramidal inputs onto parvalbumin-positive interneurons gates ocular dominance plasticity

Daniel Severin[a,1], Su Z. Hong[a,1], Seung-Eon Roh[b,1], Shiyong Huang[a], Jiechao Zhou[b], Michelle C. D. Bridi[a], Ingie Hong[b], Sachiko Murase[c], Sarah Robertson[d], Rebecca P. Haberman[e], Richard L. Huganir[b], Michela Gallagher[d], Elizabeth M. Quinlan[c], Paul Worley[b], and Alfredo Kirkwood[a,b,2]

[a]Mind/Brain Institute, Johns Hopkins University, Baltimore, MD 21218; [b]Department of Neuroscience, Johns Hopkins University, Baltimore, MD 21205; [c]Department of Biology, University of Maryland, College Park, MD 20742; [d]Department of Bioengineering, University of Maryland, College Park, MD 20742; and [e]Department of Psychological and Brain Sciences, Johns Hopkins University, Baltimore, MD 21218

Edited by Carla J. Shatz, Stanford University, Stanford, CA, and approved August 7, 2021 (received for review March 22, 2021)

Disinhibition is an obligatory initial step in the remodeling of cortical circuits by sensory experience. Our investigation on disinhibitory mechanisms in the classical model of ocular dominance plasticity uncovered an unexpected form of experience-dependent circuit plasticity. In the layer 2/3 of mouse visual cortex, monocular deprivation triggers a complete, "all-or-none," elimination of connections from pyramidal cells onto nearby parvalbumin-positive interneurons (Pyr→PV). This binary form of circuit plasticity is unique, as it is transient, local, and discrete. It lasts only 1 d, and it does not manifest as widespread changes in synaptic strength; rather, only about half of local connections are lost, and the remaining ones are not affected in strength. Mechanistically, the deprivation-induced loss of Pyr→PV is contingent on a reduction of the protein neuropentraxin2. Functionally, the loss of Pyr→PV is absolutely necessary for ocular dominance plasticity, a canonical model of deprivation-induced model of cortical remodeling. We surmise, therefore, that this all-or-none loss of local Pyr→PV circuitry gates experience-dependent cortical plasticity.

visual cortex | disinhibition | synaptic plasticity | neuropentraxin2 | NPTX2

Experience during a postnatal, critical period is essential to properly shape the functional connectivity of cortical circuits. A canonical model of cortical plasticity is the shift in ocular dominance following monocular deprivation (MD), which biases responses toward the nondeprived (ND) eye. Prior research established that MD-induced changes result from the reorganization of excitatory glutamatergic synapses onto excitatory pyramidal neurons (Pyr), which is, in turn, regulated by an inhibitory GABAergic network composed of parvalbumin-positive inhibitory interneurons (PVs). The current consensus is that a reduced, permissive level of inhibition from PV circuits in cortical layer 2/3 is required for plasticity at downstream excitatory synapses and that inhibition above or below the permissive range constrains the response to MD (1–3). Although the notion that rapid cortical disinhibition precedes and initiates the plasticity of glutamatergic connectivity is well established (4, 5), and decades old (6–8), the underlying cellular mechanisms remain unclear.

Disinhibition of excitatory cortical neurons could be achieved indirectly, for example by suppressing PV activity via enhancing inhibition from other interneurons through cholinergic neuromodulation (9, 10) but more directly, and likely more effectively, by reducing the excitatory input onto PVs (4, 11–13). Our current investigation uncovered a unique form of experience-dependent plasticity that regulates the connectivity between pyramidal neurons and PVs. We found that the initial response to MD is the functional and structural elimination of ∼50% of these connections. In contrast to the outcome of known mechanisms of synaptic plasticity that manifest in widespread graded changes in synaptic strength, the loss of pyramidal–PV connectivity occurs in a discrete, "all-or-none," fashion: whereas a subset of connections become completely eliminated, the persistent connections have normal strength. This disconnection is not only rapid but it is transient, affects only very local pyramidal–PV pairs, and, importantly, manipulations that promote/prevent this disconnection also promote/prevent shifts in ocular dominance. We surmise, therefore, that the rapid and transient disconnection of discrete subsets of PV circuits enables the subsequent Hebbian and homeostatic modification of glutamatergic circuitry.

Results

Brief MD Transiently Reduces Local Connectivity between Pyrs→PVs. We evaluated how MD affects the connectivity between pyramidal neurons and PV interneurons (Pyrs→PVs) in mouse layer 2/3. To that end, we performed visualized, whole-cell–paired recordings in slices containing the monocular zone of the primary visual cortex (V1) of mice expressing tdTomato in PVs (Fig. 1 *A* and *B* and Materials and Methods). Consistent with previous studies (11, 14), in juvenile mice (postnatal day 24 [p24] to postnatal day 30 [p30]), the connection probability in proximate Pyr→PV pairs (less than 50 μm apart) was high (∼p0.5) in slices from normal-reared (NR) mice. In mice subjected to MD for 1 d (MD1), connection probability was reduced in the V1 contralateral to the deprived eye (Fig. 1*C*) but only for the pairs

Significance

We report a unique form of neural plasticity in the visual cortex. Unlike well-known forms of neural plasticity, in which synaptic connections are slowly weakened or strengthened, we found that visual deprivation causes a rapid and transient "all-or-none" loss of local connections between pyramidal cells and parvalbumin-positive interneurons (Pyr→PV). After 1 d of visual deprivation, half of these connections are lost, whereas the spared ones remain unchanged; after 2 d of deprivation, the connectivity levels return to normal. Finally, we show that this early transient all-or-none loss of Pyr→PV connections is an obligatory step for subsequent changes in the cortical function induced by visual deprivation.

Author contributions: D.S., S.Z.H., S.-E.R., J.Z., M.C.D.B., I.H., S.M., S.R., R.P.H., E.M.Q., P.W., and A.K. designed research; D.S., S.Z.H., S.-E.R., S.H., J.Z., M.C.D.B., I.H., S.M., S.R., and R.P.H. performed research; R.L.H. and M.G. contributed new reagents/analytic tools; D.S., S.Z.H., S.-E.R., S.H., M.C.D.B., I.H., S.M., S.R., R.P.H., and E.M.Q. analyzed data; S.H. made the initial discovery; and D.S., E.M.Q., P.W., and A.K. wrote the paper.

The authors declare no competing interest.

This article is a PNAS Direct Submission.

[1]D.S., S.Z.H., and S.-E.R. contributed equally to this work.

[2]To whom correspondence may be addressed. Email: kirkwood@jhu.edu.

This article contains supporting information online at https://www.pnas.org/lookup/suppl/doi:10.1073/pnas.2105388118/-/DCSupplemental.

Published September 10, 2021.

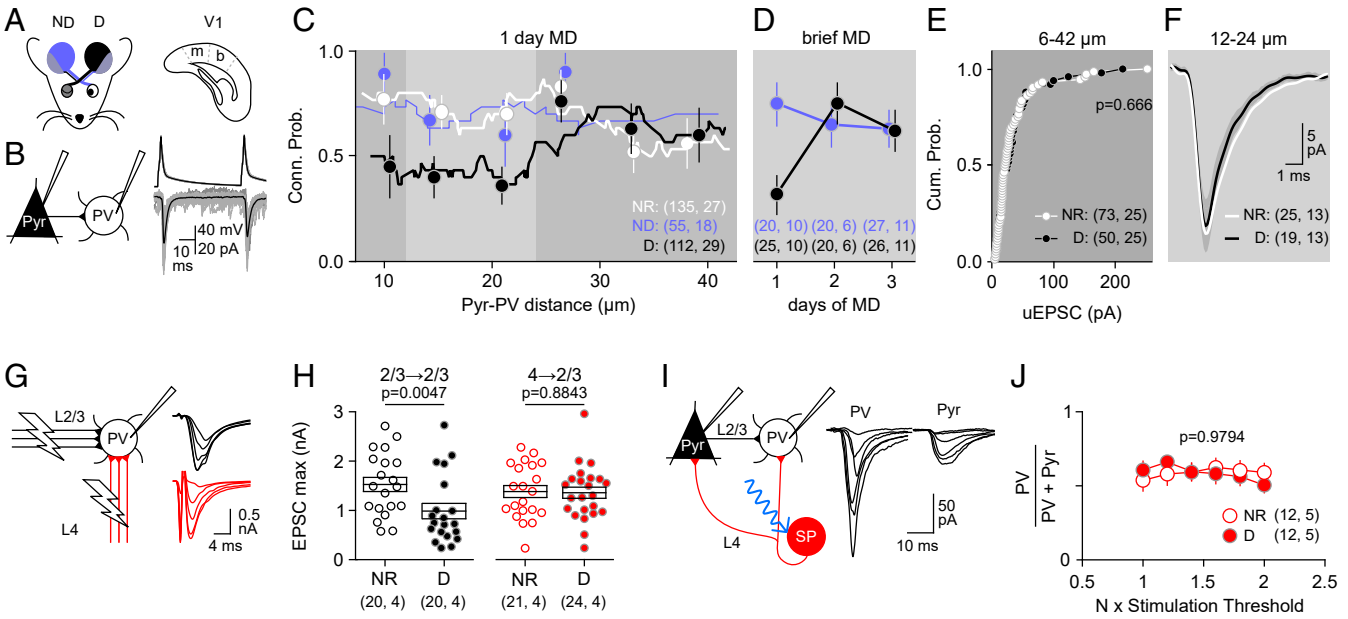

Fig. 1. MD selectively eliminates functional connections between local Pyr→PVs in Layer 2/3. (*A–F*) Changes in lateral connections. (*A*) Paired whole-cell recordings in slices containing deprived (D), ND, or NR monocular V1. (*B*) Example uEPSCs (individuals: gray; average: black) evoked in a PV by pyramidal firing. (*C*) Probability that Pyr→PV pairs are synaptically connected versus distance between somas. Lines are 21 points running averages and symbols are binned averages over 10 μm (NR: white and D [1 d]: black; ND: blue). (*D*) Transient connectivity changes during MD. The difference in pair connectivity between D and ND hemispheres was significant following 1 d of MD only [$\chi^2(3 \times 2) = 10.84$ $P = 0.0547$; F-test MD1 $P = 0.0139$; F-test MD2 $P = 0.7311$; and F-test MD3 $P > 0.9999$]. (*E* and *F*) MD does not affect the uEPSC magnitude of the connected pairs. (*E*) Distributions of the uEPSC magnitude of all connected pairs in NR (white circles) and D (black circles). Kolmogorov–Smirnov test: $P = 0.666$. (*F*) Average uEPSCs traces (± 95% CI) for all connected pairs; MD connected pairs separated by >12 μm and <24 μm (light gray zone in *C*) have comparable amplitude. Mann–Whitney *U* test (MW-test): $U = 222.5$, $P = 0.7294$). (*G–J*) MD1 does not affect ascending inputs from layer 4 onto layer 2/3 PVs. (*G*) Maximal EPSCs (EPSCmax) were computed from electrical stimulation series of increasing intensity applied to layer 2/3 (black) or layer 4 (red). (*H*) MD1 reduced the EPSCmax evoked from layer 2/3 (MW-test U = 97, $P = 0.0047$) but not from layer 4 (*t* test t = 0.1464, $P = 0.8843$). (*I*) Example EPSCs evoked in neighboring PVs and pyramidal neurons by activating layer 4 inputs with optogenetic stimulation of increasing intensities (see Materials and Methods for details). (*J*) The response ratio (PV/PV + Pyr) was similar across stimulation intensities and similar in pairs from NR (open circles) and D (filled circles) mice (ANOVA F[1,128] = 0.0007, $P = 0.9794$ and interaction F[5,128] = 0.49, $P = 0.7844$). Averages are shown as circles ± SEM.

less than ~25 μm apart. A logistic regression analysis confirmed the significance of these differences ($|Z| = 3.228$ and $P = 0.0012$), including the interaction between experience and Pyr–PV distance ($|Z| = 2.435$ and $P = 0.0149$). In contrast, MD1 did not affect the connectivity in the ND cortex ipsilateral to the deprived eye (NR–ND: $P = 0.6005$). Using this ND cortex as a control, we found that the disconnection in the deprived cortex is transient: The differences between cortices are significant after 1 d but not after 2 and 3 d of MD (logistic regression: ($|Z| = 2.370$, $P = 0.0178$ and interaction between experience and days: $|Z| = 2.020$, $P = 0.0434$; Fig. 1*D*). Importantly, the amplitude of the unitary excitatory postsynaptic current (uEPSC) of the proximal pairs that remained connected (within 12 to 24 microns) was not affected by MD (Fig. 1 *E* and *F*). Moreover, MD did not affect crucial determinants of the uEPSC amplitude, including the quantal size, failure rate, and the size and replenishment rate of the readily releasable vesicle pool (*SI Appendix*, Fig. S1 *A–H*). We found parallel changes in the binocular zone (*SI Appendix*, Fig. S6 *A* and *B*): MD1 also reduces the Pyr→PV connection probability from 0.69 ± 0.09 ($n = 5$ mice, 29 pairs) in NR mice to 0.40 ± 0.09 in MD mice ($n = 10,42$ and $P = 0.029$) and without affecting the uEPSC amplitude (NR: 18.0 ± 3.2 pA, $n = 15$ pairs; D: 19.0 ± 2.8, $n = 13$ pairs; and *t* test: 0.224, $P = 0.824$). Thus, like reported MD-induced changes in excitatory inputs onto pyramidal cells (15), the all-or-none Pyr→PV disconnection occurs in both monocular and binocular V1. To simplify interpretations, however, unless explicitly noted, most of subsequent experiments were performed in the monocular zone. Finally, we also evaluated MD-induced changes in the outputs of PVs: PV→PV and PV→Pyr. MD1 did not affect the amplitude of the maximal inhibitory postsynaptic currents (IPSCs) recorded in PVs (*SI Appendix*, Fig. S1 *I* and *J*), the proportion of connected PV→Pyr pairs, nor the amplitude of the unitary IPSCs in pyramidal neurons (*SI Appendix*, Fig. S1 *K–N*).

Layer 2/3 PVs are also driven by excitatory inputs from layer 4 (16). Since the probability of detecting connected intralaminar Pyr→PV pairs is typically very low (2 out of 20), we examined the effects of MD in two ways. First, by computing the amplitude of maximal compound EPSCs as a measure of total strength in NR and MD mice (11, 17). MD1 reduced the amplitude of the maximal EPSC recruited electrically from layer 2/3 but not the EPSC recruited from layer 4 (Fig. 1 *G* and *H*). Next, we evaluated changes in the ratio of EPSCs evoked in nearby pyramidal neurons and PVs by the optogenetic stimulation of layer 4 inputs. MD1 did not affect the EPSC ratio in PV/Pyr (Fig. 1 *I* and *J*). Inasmuch 1 d of MD does not affect excitatory inputs onto layer 2/3 pyramidal cells (4, 18), the absence of changes in the PV/Pyr ratio argues against alterations in layer 4 inputs to layer 2/3 PVs. In sum, the primary effect of brief MD on Layer 2/3 PV circuitry is the selective and complete, yet transient, all-or-none elimination of approximately half the functional connections made by nearby pyramidal cells, without affecting the potency of the remaining input connections or the PV output.

Evidence that MD Induces a Transient Structural Loss of Pyr→PV Connections. The all-or-none elimination of functional Pyr→PV connectivity is reminiscent of synaptic pruning. Hence, it suggests a loss of synaptic structure rather than a reduction in synaptic strength. To test this idea, we first considered the possibility

that MD might "silence" Pyr→PV connections by inducing the removal of synaptic AMPA receptors (AMPAR), as has been documented in other neurons. To that end, we compared the AMPAR/NMDAR EPSC ratio, an indicator of changes in silent synapses, in PVs from deprived and ND cortices. We detected no differences following MD1, arguing against a silent synapse scenario (Fig. 2 *A* and *B*). Next, we evaluated changes in the number of excitatory synapses onto PVs using immunocytochemistry to visualize the vesicular glutamate transporter 1 (VG1) as a marker for intracortical glutamatergic terminals. Since whole-cell voltage–clamp recordings are dominated by activity at perisomatic synapses, we focused on VG1 puncta in the soma and proximal dendrites of PVs. After 1 d of MD, the average number of these VG1 puncta was reduced in deprived relative to ND in both the monocular and the binocular zones, but there was no difference after 3 d of MD (Fig. 2 *C* and *D*). These results suggest that MD causes a transient structural elimination of excitatory synapses onto PVs.

NPTX2 but Not NRG1 Mediates the Disconnection of Pyrs→PVs by MD. Attractive candidate mechanisms to mediate the disconnection of Pyr→PV synapses by MD include neuropentraxin2 (NPTX2) and neuregulin1 (NRG1) signaling. Both molecules are secreted by pyramidal cells in an activity-dependent manner and promote/stabilize AMPARs at excitatory synapses onto PVs in multiple brain regions, including the visual cortex (11, 12, 19, 20). A reduced secretion of NRG1 during MD has been associated with diminished excitatory input onto PVs (13). We therefore tested whether supplemental NRG1 [1 μg subcutaneous (12)] prevents the disconnection of Pyr→PV during MD1. Systemic NRG1 did not inhibit the decrease in Pyr→PV connection probability in deprived V1 after MD1 (*SI Appendix*, Fig. S3*A*). Next, we examined how exogenous NRG1 affects excitatory inputs onto layer 2/3 PVs in slices from MD1 mice. To that end, we recorded in the same PVs the EPSCs evoked by layer 2/3 and layer 4 stimulation. NRG1 application specifically enhanced the inputs from layer 4 (*SI Appendix*, Fig. S3*B*), which are normally not affected by MD (see Fig. 1). A comparable enhancement of layer 4 inputs was also observed in NR V1b (*SI Appendix*, Fig. S3*C*). Together, this argues against a role for NRG1 in the elimination of Pyr→PV connections in layer 2/3 by MD1.

The genetic ablation of NPTX2 (also known as NARP) has been shown to result in the all-or-none elimination of a substantial proportion of Pyr→PV connections (11). To examine the role of NPTX2 in the disconnection induced by MD, we monitored how MD changes the release NPTX2 in vivo. NPTX2 release was monitored by the viral expression of NPTX2 fused with super ecliptic pHlurorin (SEP), which fluoresces only in the extracellular compartment (21). In wild-type mice virally transfected with AAV-CaMKII-NPTX2-SEP in V1, two-photon (2P) imaging in the superficial cortical layers of revealed discrete puncta (2 to 3 μm), likely representing extracellular aggregates of NPTX2-SEP (Fig. 3 *A* and *B*). One day of MD substantially reduced the density and intensity of these puncta, which returned to normal levels by the second day of MD (Fig. 3 *B–D*). A reduction in NPTX2 protein content in V1 after 1 d of MD is also revealed by quantitative immunohistochemistry (Fig. 3 *E* and *F*) and Western blot analysis (*SI Appendix*, Fig. S4). These results suggest that MD transiently reduces the expression of NPTX2.

To test whether an MD-induced reduction in NPTX2 content is necessary for the Pyr→PV disconnection, we exploited the fact that the effects of MD on Pyr→PV-IN inputs have a critical period. The loss of connectivity induced by 1 d of MF are robust up to p50 but cannot be elicited at ~p100 (Fig. 3*G*). We therefore tested whether the overexpression of NPTX2 prevents the MD-induced Pyr→PV disconnection in juveniles and whether reducing the functionality of NPTX2 enables the disconnection in adults. In the first case, we transfected V1 neonatally with AAV-CaMKII-NPTX2-SEP; in the second case, we transfected V1 in adults (p80 to p90) with AAV2/2.CAMKII.dnNPTX2.EGFP to express a dominant, negative form of NPTX2 that disrupts biosynthesis of the native NPTX1/2/R complex (22). In juveniles (p21 to p25) overexpressing NPTX2-SEP, the Pyr→PV connectivity remained high after MD1, comparable to age-matched NR controls in V1m (Fig. 3*H*) and also in V1b (*SI Appendix*, Fig. S6). As a control, we confirmed reduced connectivity after MD1 in juveniles transfected with the same serotype AA virus expressing GFP (AAV2-CaMKII-GFP). On the other hand, in postcritical period adults (~p110), the expression of dnNPTX2, which by itself did not affect the Pyr→PV connectivity, enabled a substantial and significant disconnection of Pyr→PV inputs following MD1 (Fig. 3*I*). These results support a model in which a reduction of NPTX2 is a necessary permissive factor for the MD-induced disconnection of Pyr→PV inputs in layer 2/3.

Manipulation of NPTX2 Prevent/Enables Ocular Dominance Plasticity. Finally, we examined whether the manipulations of NPTX2 that prevent/enable the Pyr→PV disconnections also prevent/enable the plasticity of ocular dominance (ODP) induced by MD. In mice, ODP induced by MD has a critical period with a time course parallel to the time course for MD-induced disconnections of Pyr→PV inputs in layer 2/3 (Fig. 4*A*). ODP in the critical period is manifest as a rapid reduction of cortical responsiveness to the deprived eye in juveniles (younger than ~p35) and a delayed increase responsiveness to the ND eye in young adults (younger than ~p70 (23, 24). We asked, therefore, how the overexpression of NPTX2 following neonatal viral transfection (as in Fig. 3*H* and *SI Appendix*, Fig. S6), affects ocular dominance shift induced by brief MD in juveniles (3 d; Fig. 4*A*). We used intrinsic signal imaging (ISI) to evaluate cortical responses

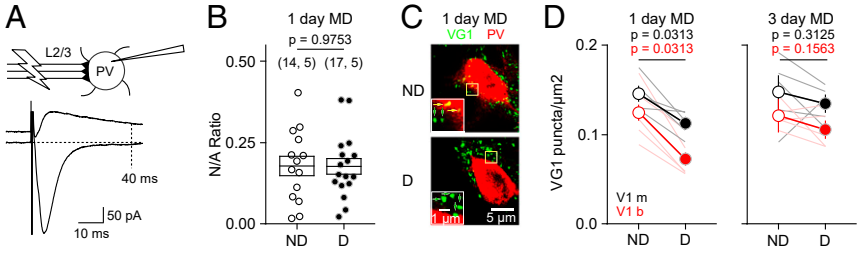

Fig. 2. MD1 induces a transient loss of structural Pyr→PV connections. (*A* and *B*) Evidence against change in silent synapses. (*A*) Schematic for measurement of NMDAR and AMPAR EPSCs. (*B*) MD1 does not affect the NMDAR/AMPAR (N/A) EPSC amplitude ratio (*t* test F[29] = 0.03165, *P* = 0.9750). The number of cells and mice are indicated in parentheses. (*C* and *D*) Immunohistochemical analysis of the MD-induced changes in the VGlut1 puncta density (VG1) on the soma and proximal dendrites of layer 2/3 PVs. (*C*) Example cases (single z plane) showing PV in red, VG1 in green, 40× mag. Area in yellow box is magnified 2× in inset. Colocalized yellow puncta are yellow arrows and noncolocalized puncta are green arrows (see *SI Appendix*, Fig. S2 for details). (*D*) Quantification of colocalized PV + VG1. Thin lines connect the results of the deprived (D) and ND V1 monocular (black) or binocular (red) of the same mouse after MD for 1 d (*Left*) or 3 d (*Right*). Averages are shown as circles connected by thick lines ± SEM. *P* = paired *t* test.

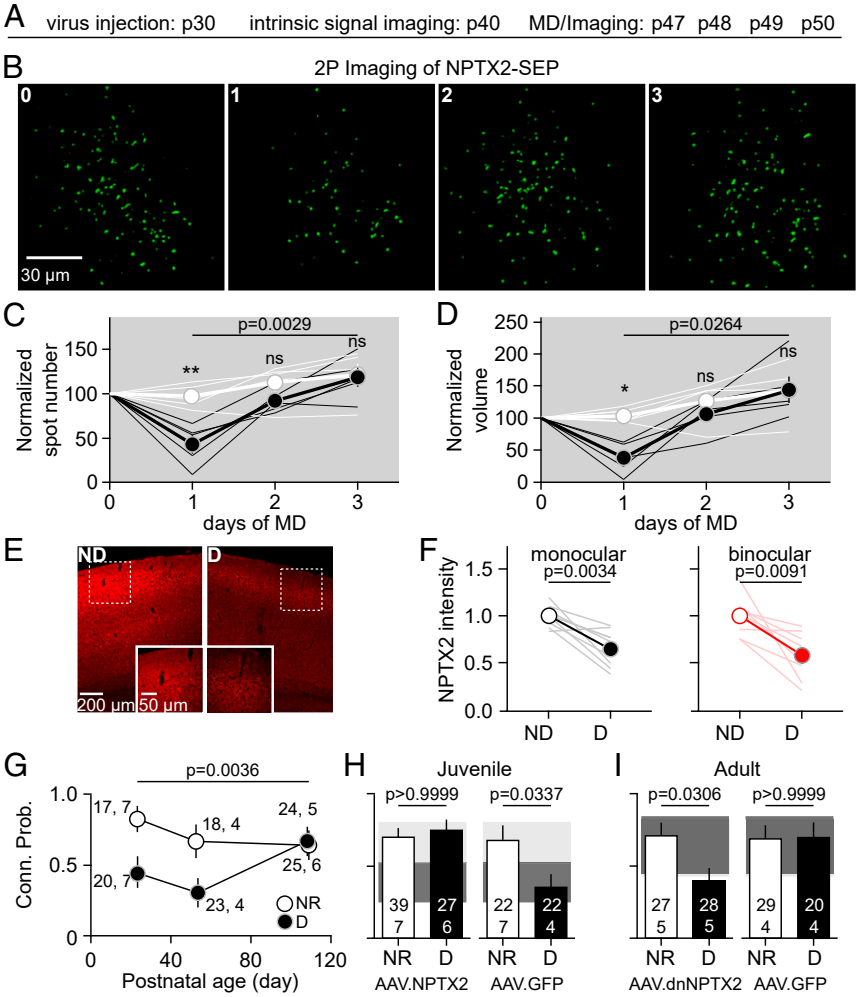

Fig. 3. MD-induced disconnections depend on reduced NPTX2 content. (*A–D*) MD transiently reduces surface Nptx2 in layer 2/3 (L2/3) V1. (*A*) Experimental schedule. (*B*) Example images from the same mouse before and after 1 to 3 d of MD reveals a reduction of the number of NPTX2-SEP puncta at day 1. (*C* and *D*) Quantification of NPTX2-SEP fluorescence in L2/3 (80 to 180 µm) in deprived (black) and ND (white) mice indicates a significant and transient reduction at day 1 in spot number (*C*) and volume (*D*). The lines in *C* and *D* represent data from individual mice and the circles and lines represent average ± SEM. The asterisk indicates significant pairs (Sidak's test after a two-way ANOVA). (*E* and *F*) MD1 lowers NPTX2 immunostaining in V1 of young mice (p21 to p23). (*E*) Example case of deprived and ND visual cortices in the same mice. (*F*) Quantification of NPTX2. Thin lines connect results of the deprived (D) and ND V1 monocular (black) or binocular (red) of the same mouse after MD1. Averages are shown as circles connected by thick lines ± SEM. *P* = paired *t* test. (*G–I*) Manipulations of NPTX2 prevent/enable MD-induced Pyr→PV disconnection (*G*) In mice younger than ~p60 but not in ~p110 mice, MD1 reduces the probability of connection (logistic regression F[1,23] = 8.835, *P* = 0.0036 and interaction F[1,23] = 3.918, *P* = 0.0500). (*H* and *I*) Transfection with AAV2-CaMKII-NPTX2-SEP at birth prevents the MD1-induced disconnection of Pyr→PV inputs in juvenile mice (*H*), whereas in adult mice the transfection with AAV2-dnNPTX2 enables the MD1-induced disconnection (*I*). Graphs in *H* and *I* show the Pyr→PV connection probability in NR and deprived (D) mice transfected with either experimental virus (*Left*) or control virus (*Right*) (AA2-GFP). *P* values in *H* and *I* were returned by a Fisher's exact test. Filled boxes in *H* and *I* depict the 95% CI range nontransfected mice (light gray: NR and dark gray: deprived). In *E–G*, the number of cells or cell pairs and mice are indicated in parentheses, and average data are show with ± SEM.

in the binocular zone of V1, as described (25, 26). Cortical responses in mice are normally biased toward the contralateral eye and this bias is reduced by MD, reflected as a shift of the ocular dominance index (ODI; see Materials and Methods). That shift did not occur in NPTX2-transfected mice, in which the ODI for NR and MD individuals was similar (Fig. 4*B*) and within the range for NR nontransfected mice (Fig. 4*B*, light gray bar). On the other hand, mice transfected with control AAV and subjected to MD3 exhibited a reduction in ODI, comparable to the decrease in ODI induced by MD3 in noninfected controls (Fig. 4*B*, dark gray bar). In a complementary study, we determined that transfecting adult mice (>p110) with AAV-dnNPTX2 to reduce NPTX2 function (as in Fig. 3*I*) enables a juvenile-like decrease in ODI in response to MD. In these experiments, we imaged V1b before and after MD3 (Fig. 4 *C* and *D*) and confirmed that the reduction in ODI was juvenile-like; that is, it resulted from a reduction in the contralateral response, not from an increase in the ipsilateral response (Fig. 4 *E–G*). The ODI shift did not occur in adults transfected with control virus (Fig. 4*G*). Altogether, the results support the idea that a reduction of NPTX2 and the consequent loss of Pyr→PV-IN connectivity are obligatory early steps in ODP.

Discussion

Deprivation studies indicate that the rapid disinhibition of pyramidal neurons enables the plasticity of glutamatergic networks. Here, we describe a unique form of synaptic plasticity that mediates cortical disinhibition induced by MD: the all-or-none elimination of a subset of Pyr→PV connections. This all-or-none elimination of Pyr→PV inputs is distinct from most other models of synaptic weakening, in that all synaptic contacts between

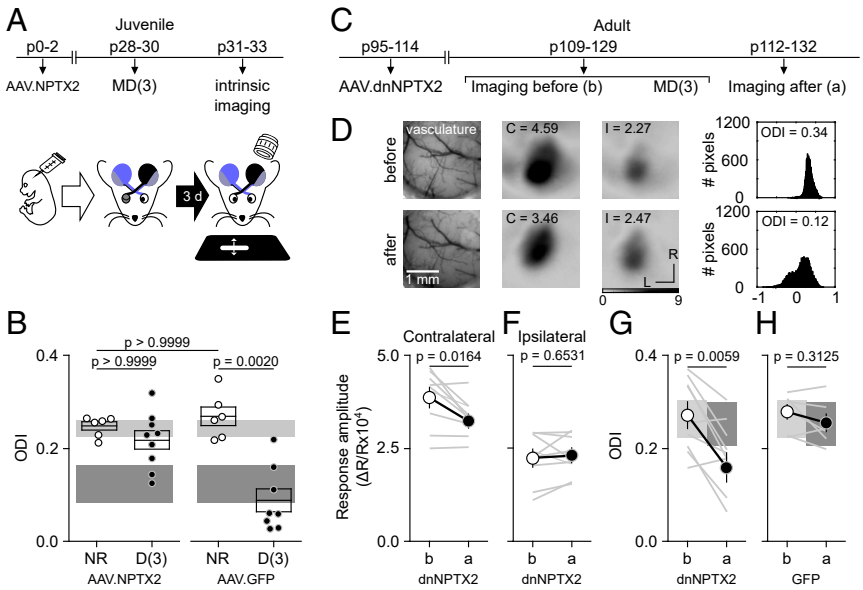

Fig. 4. Manipulation of NPTX2 can gate ODP. (*A* and *B*) Overexpression of NPTX2 prevents ODP in juveniles. (*A*) Mice were transfected at birth (p0 to p2) with AAV2-CaMKII-NPTX2-SEP or AAV2-GPP. Following 3 d of MD starting at p30 to p31, intrinsic signal responses to stimulation in each eye were recorded in the V1 contralateral to the deprived eye (see Materials and Methods). (*B*) In NPTX2-transfected mice, the ODI (see Materials and Methods) after MD3 was comparable to ND transfected mice (white circles), and it was reduced in deprived mice transfected with control (AAV2-GFP. Kolmogorov–Smirnov test K = 12.56, $P = 0.0013$ and Dunns multiple pairs comparison). For comparison, boxes in *B* depict the 95% CI range of ODI of 44 NR and 8 D nontransfected juvenile mice after MD1 (light gray: NR and dark gray: deprived). (*C*–*G*) Expression of dnNPTX2 enables juvenile-like ODP in adults. (*C*) Adult mice were transfected (p110 to p118) with AAV2-dnNPTX2. The intrinsic signal responses to stimulation in each eye were recorded in the V1 contralateral to the deprived eye before and after 3 d of MD starting at p109 to p129. (*D*) Example experiment. (*Left*) Vasculature pattern of the imaged region used for alignment. (*Middle*) Magnitude map of the visual response from the eye contralateral (C) or ipsilateral (I) to the imaged hemisphere. (*Bottom*) Gray scale response magnitude as fractional change in reflection $\times 10^4$. Arrows: L is lateral and R is rostral. (*Right*) Histogram of ODI is illustrated in the number of pixels (*x*-axis: ODI and *y*-axis: number of pixels). (*E*–*H*) Summary of changes in the response amplitude of the deprived contralateral eye (*E*), the ND ipsilateral eye (*F*), and the change of ODI (*G*) before (b) and after (a) MD. (*H*) ODI changes in adult mice infected with control GFP virus. Thin lines in *E*–*H* are individual experiments and thick line and symbols are average ± SEM. For comparison, boxes in *G* and *H* depict the 95% CI range of ODI of 15 nontransfected adult mice (light gray: NR and dark gray: deprived).

affected pairs of neurons are lost. Pyr→PV synapse elimination also contrasts with perinatal pruning of exuberant inputs (27–29) in that it is transient, lasting only 1 d, and it is not accompanied by a compensatory increase in the strength of the remaining inputs. In addition, the elimination of Pyr→PV inputs is also unique in that it is highly specific, affecting only inputs from nearby layer 2/3 Pyr and leaving inputs from distant Pyr in layer 2/3 or in layer 4 unchanged. Finally, the Pyr→PV input elimination is contingent on a reduced NPTX2 content, and it is a seemingly obligatory step for subsequent changes in ocular dominance.

The observation that the MD-induced change in Pyr→PV-IN inputs is both all-or-none and transient is somewhat counter intuitive, and it is unclear how temporary input elimination best serves ODP. Nevertheless, it seems plausible that the process is initiated by changes in neural activity resulting from diminished visual drive during MD. A reduced correlation of prepostsynaptic activity in Pyr→PV pairs after MD is expected to induce associative long-term synaptic depression (LTD) in these connections (30, 31) and may promote synapse elimination, as reported in other types of depressed synapses (32–34). We propose that the reduction in the availability of NPTX2 induced by MD contributes to the destabilization of depressed Pyr→PV inputs in V1. Notably, associative LTD in Pyr→PV connections and synapse elimination in CA1 pyramidal cells require mGluR5 activation (31, 35), raising the possibility that the elimination of individual synapses and cell-to-cell connections share common initial mechanisms. The elimination of Pyr→PV inputs is highly local, occurring only in layer 2/3 Pyr→PV pairs separated by less than ∼25 μm. This spatial requirement matches the diameter of recently reported microcolumns in the mouse cortex, suggesting that the distribution of disconnected synapses might reflect the coregulation of locally connected neuronal networks (36). The preferential, local elimination might also be attributed to cortical retinotopy, as the decrease in correlated activity during MD might be more pronounced in proximal than distal pairs. The absence of an overt change in connectivity between layer 4 Pyrs→layer 2/3 PVs following MD may be due to the low expression of NPTX2 in layer 4 neurons (Allen Brain Mouse Atlas). Finally, the loss Pyr→PV inputs might be transient because subsequent homeostatic changes in glutamatergic synapses might restore patterns of neural activity conducive to reestablish connectivity (37–40).

Previous studies, including ours (12, 13), have implicated the growth factor NRG1 in plastic changes induced in MD. In contrast, here we show that the application of exogenous NRG1 neither prevented nor restored the transient disconnection of MD-induced local Pyr→PV inputs in layer 2/3, arguing against a direct role of NRG1 in this process. A recent report utilizing a glutamate uncaging approach reported that the applied NRG1 can restore a widespread reduction of excitatory input onto layer 2/3 PVs induced by MD1 (13). However, the uncaging approach can recruit and record responses with a large polysynaptic component, and the paired whole-cell recordings used here may be preferable for resolving local monosynaptic connections. An attractive and simple possibility to reconcile these apparent discrepancies is that MD induces an NPTX-dependent disconnection of local Pyr-PV inputs in layer 2/3 and an NRG1-dependent reduction in local excitatory inputs onto layer 4 PVs. This would be in line with the notion that distinct mechanisms govern synaptic plasticity in different cortical layers (41–43) and is consistent with our observation that NRG1 affects excitatory inputs onto layer 2/3 PVs originating from layer 4 but not layer 2/3. If correct, this scenario allows for two molecularly distinct mechanisms to regulate

excitatory inputs onto PVs that are anatomically segregated, thereby minimizing functional redundancy.

The rapid and transient elimination of ∼50% of the local excitatory inputs onto PVs is likely a major determinant of the deprivation-induced cortical disinhibition attributed to the reduced activity of PVs (4, 44). However, other mechanisms might also contribute. For example, even if the strength and connectivity of the PV output is not affected by MD1 (*SI Appendix*, Fig. S1), changes in short-term synaptic dynamics, normally tuned for high-frequency transmission (45), could enhance cortical activity. Similarly, changes in the electrical coupling between PVs and tonic inhibition, known to be affected by deprivation in pyramidal neurons (46), could also enhance cortical activity. On the other hand, unlike the case of barrel cortex (47), changes in the intrinsic excitability of layer2/3 PVs are not a factor for disinhibition (13).

The critical periods for ODP and the plasticity of Pyr→PV connectivity are highly coincidental, both terminating by p90. Furthermore, manipulations of NPTX2 function that prevent and promote the transient disconnection of Pyr→PV inputs also prevent/promote ocular dominance shift after MD. We therefore surmise that the transient elimination of local Pyr→PV inputs is an obligatory initial step for the subsequent remodeling of glutamatergic circuitry underlying ODP.

An attractive candidate step to follow the loss of Pyr→PV connections could be a rapid increase in the proportion of synaptic GluN2b over GluN2a subunit, which is observed after brief visual deprivation (37, 48). The change in NMDAR composition lowers the threshold for the induction of synaptic plasticity, including LTD elicited with spike-timing protocols, and is a consequence of cortical disinhibition (37, 48). In this scenario, glutamatergic connectivity would not be intrinsically more plastic during the critical period, but plasticity is enabled by the change in GluN2b/GluN2a following the local elimination of Pyr→PV inputs. The termination of the critical period for ODP would, therefore, be a direct consequence of the loss of plasticity of the Pyr→PV inputs. In this general context, it will be of interest to determine whether the all-or-none disconnection of Pyr→PV inputs also regulates other candidate mechanisms of ODP, like the abundance of silent synapses (49). Finally, it will be also of interest to examine whether the disconnection of local Pyr→PV inputs contributes to the changes in cortical criticality after MD (44) and to the pathology in neurological conditions known to exhibit marked alterations in NPTX2 abundance, including Alzheimer's disease and schizophrenia (50).

Materials and Methods

Animals.

Mouse lines. C57BL/6, PV-cre;Ai14, Scnn1a-Tg3-cre;Ai32;PV-tdT, and Scnn1a-Tg3-cre;G42 mice of both sexes were used. All subjects were group housed (five or fewer per cage) on a 12-h light/dark cycle, with food and water available ad libitum. All protocols and procedures conformed to the guidelines of the US Department of Health and Human Services Office of Laboratory Animal Welfare and were approved by the Institutional Animal Care and Use Committees of the University of Maryland, Johns Hopkins University, or both. These committees followed the guidelines established by the Animal Care Act and NIH. For specific optogenetic stimulation in layer 4, we developed a triple transgenic line crossing the L4-Cre mouse line with the Ai32 mouse line that has a conditional allele of Rosa-CAG-LSL-ChR2(H134R)-EYFP-WPRE to drive ChR2/EYFP fusion protein expression in L4 principal cells. We then crossed L4-cre positive and Ai32 homozygous mice with PV-tdT mice.

MD. Naive mice were monocularly deprived of vision for 1, 2, or 3 d beginning at p21 to p25, p27 to p31, p50 to p54, or p100 to p118. Mice were age-matched across groups. MD (lid suture) was performed under isoflurane anesthesia (2 to 3% for induction and 1.5% for maintenance). The margins of the upper and lower lids of one eye were trimmed and sutured together. Neosporin was applied to the sutured eye. Animals were disqualified in the event of suture opening or infection.

Drug administration. The recombinant human NRG1-β1/HRG1-β1EGF domain (7.5 kDa; R&D Systems), corresponding to residues 176 to 246 of the soluble EGF domain of neuregulin β1 common to all NRG1 splice variants, was dissolved in sterile saline. We used residues 177 to 241 from the same splice variant in some cases, with no difference in results between the two peptides (7.5 kDa; ProSpec Protein Specialists). Monocularly deprived mice were subcutaneously administered with two injections of recombinant NRG1 (1 μg NRG1 in 50 μL sterile saline per injection per mouse). The first injection was applied immediately before lid suture, and the second, 1 h before the animal was euthanized for electrophysiological experiments.

Viral injections. Mice were anesthetized and head fixed in a stereotaxic device (Kopf Instruments) under 1.5 to 2% isoflurane. V1 was located in the left hemisphere using stereotaxic coordinates (3.6 mm posterior and 2.5 mm lateral to bregma). When the bregma–lambda distance was different from 4.2 mm, the stereotaxic coordinates were scaled. A craniotomy (∼0.5 mm) was made, and the virus was injected (600 nL and 100 nL/s) into layer 2/3 or layer 4 (0.3 or 0.4 mm from the cortical surface, respectively) 10 to 35 d before experimentation. For 2P imaging, during craniotomy, AAV2.CaMKII.NPTX2-SEP was injected into three sites (100 nL per site and 5 nL/s). Viral injection of AAV2.CamKII.NPTX2-SEP or AAV2.CaMKII.GFP was done by bulk regional viral injection to the visual cortical area of neonatal PV-Cre;Ai14 mice at p0 to p2 (51). Briefly, neonatal mice were cryoanesthetized in an ice-cold chamber, positioned dorsal side up, and secured with an adhesive bandage across the upper body. The visual cortical area was targeted with anatomical landmarks, including occipital fontanelle and lambdoid suture, visible through the neonatal skin. A total of 600 nL AAVs were injected right beneath the skull with a syringe infusion pump (50 nL/s). After the injection, mice were kept on a heating pad and returned to their home cage once recovered. For optical imaging of intrinsic signaling, AAVs were injected at three locations targeting layer 2/3 of the binocular region of the V1 (500 nL/each injection site). For 2P imaging, during craniotomy, AAV2-CaMKII-NPTX2-SEP was injected into three sites (100 nL per site) using a glass pipette (pulled by pipette puller, Narishige) and Nanoject (Drummond Scientific Company) at a rate of 5 nL/s.

Electrophysiology.

Slice preparation and recording. Visual cortical slices 300-μm thick were prepared as previously described (11). Each mouse was anesthetized using isoflurane vapors. Mice older than p50 were transcardially perfused with ice-cold dissection buffer containing (in millimolar): 212.7 sucrose, 5 KCl, 1.25 NaH_2PO_4, 10 MgCl2, 0.5 CaCl2, 26 NaHCO3, and 10 dextrose, bubbled with 95% O2/5% CO_2 (pH 7.4). The slices were transferred to artificial cerebrospinal fluid (ACSF), incubated at 30 °C for 30 min, and then kept at room temperature for 30 min until they were transferred to the recording chamber. ACSF was similar to dissection buffer except that sucrose was replaced by 124 mM NaCl, MgCl2 was lowered to 1 mM, and CaCl2 was raised to 2 mM. Visualized whole-cell recordings were made from PVs and pyramidal neurons with glass pipettes filled with 130 mM K-gluconate, 10 mM KCl, 10 mM Hepes, 0.2 mM EGTA, 0.5 mM Na3GTP, 4 mM MgATP, and 10 mM Na-Phosphocreatine (pH 7.2 to 7.3 and 280 to 290 mOsm). Only cells with series resistance <25 MΩ (with <20% variation over the experiment) were included. Data were filtered at 4 kHz and digitized at 10 kHz using Igor Pro (Wave Metrics). The intersomatic distance was calculated as the Euclidean distance between the centers of both somata. uEPSCs were recorded in voltage–clamp in the PV-INs at −70 mV and evoked by suprathreshold somatic current injection (2 ms) in presynaptic pyramidal neurons. uIPSCs were recorded in voltage–clamp in pyramidal neurons at 0 mV and evoked by suprathreshold somatic current injection (2 ms) in presynaptic PVs. For presynaptic parameters, all presynaptic cells were depolarized with 1.7 pA current injection. At least 20 responses evoked at 0.1 Hz with paired pulse stimulation (interstimulus interval: 50 ms for Pyr→PV pairs and 100 ms for PV→Pyr pairs) were used to confirm a synaptic connection and to compute the amplitudes of the unitary responses. When the temporal course of evoked EPSCs was measured (*SI Appendix*, Fig. S3 *B* and *C*), recordings were excluded if baselines were not stable. No more than eight cell pairs were recorded per animal.

Mean–variance and presynaptic analysis. Mean–variance and presynaptic analysis were performed on responses evoked by at least 15 stimuli trains delivered at 50 Hz and 20 s intervals. The uEPSC amplitude was measured for each stimulus, and the mean and variance were plotted against each other. Quantal size (q) was obtained from the linear regression slope for all events, excluding the two events with the highest average release probability (52). To quantify the readily releasable pool (RRP) we used a linear fit of the relation between the cumulative amplitude and the stimulus number (53). In this model, the RRP replenishment rate and the RRP size are given by the slope and the intercept of the linear fit. We considered only those cases in which the R^2 value of the fit was >0.95 for presynaptic analysis and >0.5 for mean–variance analysis.

Maximal postsynaptic currents. Maximal postsynaptic currents (PSC max) recorded in PV-IN were evoked every 15 s by electrical stimulation using a theta glass bipolar electrode placed in the middle of the cortical thickness. We used a Cs-gluconate–based internal solution containing (in millimolar) 120 Cs-gluconate, 8 KCl, 10 Hepes, 1.12 EGTA, 0.5 Na3GTP, 4 Na2ATP, 10 Na-phosphocreatine, and 5 lidocaine; pH 7.2 to 7.3, and 280 to 290 mOsm. Excitatory and inhibitory PSC max (EPSC and IPSC max) were recorded in voltage–clamp at −40 and −70 mV, respectively. For IPSC max measurements, 25 μM 6-cyano-7-nitroquinoxaline-2,3-dione (CNQX) and 100 μM DL-2-amino-5 phosphonopentanoic acid were included in the bath, and electrode capacitance and series resistance were compensated (prediction 90%, correction 80 to 85%, and bandwidth 3 kHz).

NMDA/AMPA ratios. NMDA/AMPA ratios were calculated from excitatory currents onto PV-IN evoked from layer 2/3 by electrical stimulation. Two times the stimulus intensity that evoked the minimal AMPA response was used. An internal solution containing (in millimolar) 102 cesium gluconate, 5 TEA chloride, 3.7 NaCl, 20 Hepes, 0.3 Na-GTP, 4 Mg-ATP, 0.2 EGTA, 10 BAPTA, 5 QX-314 (pH 7.2, ∼300 mOsm) under voltage–clamp (Vh = −70 mV for AMPA and Vh = +40 mV for NMDA). To isolate glutamate evoked currents and minimize multisynaptic responses, ACSF in the recording chamber contained 2.5 μM gabazine, 25 μM CNQX, 10 μM adenosine, 4 mM CaCl2, and 4 mM MgCl2.

PV/Pyr EPSC response ratios. PV/Pyr EPSC response ratios were calculated from L4-evoked excitation onto layer 2/3 PV-IN and the neighboring pyramidal cell (12 to 24 μm apart). An input–output curve for excitatory postsynaptic potentials onto each cell was measured by simultaneous pair recordings using identical light intensity. The stimulation threshold was defined as the light intensity that elicited the minimal PV response with no failures.

Immunohistochemistry.

VGluT1 immunohistochemistry. Subjects were anesthetized with isoflurane and perfused with phosphate-buffered saline (PBS), followed by 4% paraformaldehyde (PFA) in PBS. Brain was postfixed in 4% PFA for 24 h followed by 30% sucrose for 24 h and cryoprotectant solution (0.58 M sucrose, 30% [vol/vol] ethylene glycol, 3 mM sodium azide, 0.64 M sodium phosphate, pH 7.4) for 24 h. Coronal sections (40 μm) were made on a Leica-freezing microtome (Model SM 2000R). Sections were blocked with 4% normal goat serum in 1× PBS for 1 h. Antibodies were presented in a blocking solution for 18 h, followed by appropriate secondary antibodies.

VGluT1 antibodies. The following antibodies/dilutions were used: mouse anti-parvalbumin (PV, Millipore) RRID:AB_2174013, 1:2,000; guinea pig anti-VGluT1 (Millipore) RRID:AB_2301751, 1:2,000; and followed by appropriate secondary IgG conjugated to Alexa-488, 546 (Thermo Fisher Scientific) RRID:AB_2534089, RRID:AB_2534093, and RRID:AB_2535805, 1:1,000.

VGluT1 imaging and analysis. Images were acquired on a Zeiss LSM 980 confocal microscope with Airyscan mode using the optimal z-interval (0.18 μm) with a 40× lens (Zeiss Plan-neofluar 40×/1.3 Oil DIC, NA = 1.3) and deconvoluted using "Airyscan processing" function in "ZEN" software. PV + somata were identified by size exclusion (20 to 200 μm^2) and fluorescence intensity (autothreshold + 25). The colocalization of VGluT1 puncta on PV somata were analyzed in single z section images taken at 40× using Fiji. After the threshold function was applied to VGluT1 puncta (autothreshold+25), colocalized puncta were identified by size exclusion (0.1 < 2.0 μm^2). To minimize false positive colocalization, only colocalized puncta that appear in more than two adjacent z sections were quantified.

NPTX2 immunohistochemistry. Monocular-deprived mice (day 1) were perfused with 4% PFA, and the brains were incubated with 4% PFA overnight and then with 30% sucrose in PBS for 3 d. A total of 20 μm coronal sections that include V1 monocular and binocular regions were made with cryostat (Leica). Tissues were incubated in sodium citrate buffer (10 mM) with 0.05% Triton X-100 (pH 6.0) for antigen retrieval at 80 °C, followed by permeabilization in 1% Triton X-100. After blocking in 10% normal serum, 1% BSA, and 0.3% Triton X-100, tissues were incubated with rabbit NPTX2 polyclonal antibody (1:250) overnight at 4 °C, described previously (XIAO), and then with anti-rabbit alexa-555 secondary antibody (1:200) (Invitrogen AB_2633281) for 1.5 h at room temperature. Images were taken using LSM 880 (Zeiss) with 5× or 25× lens.

NPTX2 quantification. NPTX2 immunoreactivity was compared between monocular-deprived hemisphere and ND hemisphere for both monocular and binocular regions. Quantification was performed blinded to which eye was sutured. Layer 2/3 regions (100 to 300 μm from dura) were measured for intensity and background subtracted with intensity in layer 4 (300 to 400 μm from dura) using ImageJ. Intensities of four sections were averaged per mouse. The intensity in monocular-deprived hemisphere was normalized to the intensity in ND hemisphere for comparison.

Western blots. Protein from the dissected visual cortex was extracted with radioimmunoprecipitation assay buffer, such that the ND hemisphere was used as a control for each deprived side of the mouse. A total of 12 μg protein was run on 4 to 12% Nupage gels and transferred to nitrocellulose membrane. Membranes were probed Nptx2 (1:1,000; Abcam: ab191563) and visualized a chicken anti-rabbit IgG, Alexa Fluor 647 secondary antibody (Thermo Fisher Scientific: A-21443). Tubulin was used as a loading control (α-tubulin mouse mAb; Cell Signaling: cat# 3873). Fluorescent bands were visualized on Typhoon 9410 variable mode imager (Amersham), with settings optimized for linear detection of Nptx2 and tubulin band intensities. Scans were quantified using ImageQuant with a fixed area for each protein. Background-subtracted average intensities were *z*-scored to combine across gels.

Imaging.

Craniotomy. To install the glass window, juvenile mice (p27 to p31) were first anesthetized with isoflurane (2.5% for induction and 1.5% for maintenance in oxygen). After removal of the skin, connective tissue was gently removed by the blade with hydroperoxide. Translucent dental cement (C&B metabond) was applied to the exposed dry skull region. A 3-mm diameter craniotomy was made with a No. 11 surgical blade over the putative visual cortical area, and the virus injection was made when corresponded. Three-layered (one 5-mm and two 3-mm glass cover glass) glass window was installed to the craniotomy, and dental cement was applied to fix the window. For 2P microscopy, the custom-made metal head bar was attached using the dental cement Superbond (Sun Medical). For the older animals (∼p90), a craniotomy was performed with a dental drill. Atropine (0.05 mg/kg, subcutaneous [s.c.]) and dexamethasone (4.8 mg/kg, intramuscular [i.m.]) were injected to reduce mucosal secretion and brain edema, respectively.

Optical imaging of the intrinsic signal. Optical imaging of the intrinsic signal was performed with the mice anesthetized with isoflurane (2 to 3% for induction and 0.7 to 1.2% for maintenance in oxygen) supplemented with chlorprothixene (2 mg/kg, i.p.). The mice were placed with head fixed in front of the liquid crystal display monitor for visual stimulus. Atropine was injected subcutaneously to reduce mucosal secretion (0.05 mg/kg). Eye drops were administered to keep eyes moist, and body temperature was maintained at 37 °C with a heating pad and a rectal probe. Heart rate was monitored throughout the experiment by electrocardiogram. The acquisition of intrinsic signal was performed following the method optimized to measure the ocular dominance in mice (54). Briefly, visual stimulation evoked intrinsic signals were acquired using a Dalsa 1M30 charge-coupled device (CCD) camera (Dalsa) controlled by custom software. The surface vasculature and EYFP fluorescence were visualized with 555-nm light-emitting diodes (LED) illumination, and the intrinsic signals were imaged with 610-nm LED illumination. For the acquisition of the intrinsic signal, the camera was focused 600 μm below the surface of the skull. An additional red filter was interposed to the CCD camera, and intrinsic signal images were acquired. A high-refresh rate monitor (1,024 × 768 at 120 Hz; ViewSonic) was placed 25 cm in front of the mouse, with their midline aligned to the midline of the mouse for visual stimulus. The visual stimulus presented was restricted to the binocular visual field (−5° to +15° azimuth) and consisted of a thin horizontal bar (height = 2° and width = 20°) continuously presented for 5 min in upward (90°) and downward (270°) directions to each eye separately. The cortical response at the stimulus frequency was extracted by Fourier analysis. The two maps generated with the opposite direction of the drifting bar were averaged for each eye to calculate the response amplitude and the ODI. The ODI was computed as follows: 1) the intensity maps were smoothed by 5 × 5 low-pass Gaussian filter; 2) the binocular region of interest (ROI) was defined at 30% of peak response amplitude of the smoothed intensity map from the ipsilateral eye; 3) the response amplitude of each eye was calculated by averaging the intensity of all pixels in the ROI; and 4) the ODI was calculated by the average of (C − I)/(C + I) of all pixels in the ROI, in which C and I are the contralateral (C) and ipsilateral (I) eye, respectively.

In vivo 2P awake microscopy for NPTX2-SEP imaging. Confocal microscopy was performed with a laser-scanning microscope (Olympus) equipped with an ultrasensitive gallium arsenide phosphide detector (Hamamatsu) and a Galvanometer scanner (Thorlabs). 2P excitation was carried out by ultrafast Ti:Sapphire laser Mai Tai eHP DeepSee (Spectra-Physics), operating the wavelength at 920 nm for visualizing NPTX2-SEP with GFP filter using 20× objective XLUMPLFL20XW (Olympus). Hardware operation and image acquisition were performed with PrairieView software (Bruker). Around 11 to 13 d after surgery, mice were handled for 10 to 15 min and acclimated to the imaging setup for 15 to 30 min by fixing their head bars to the custom-made head fixation apparatus and imaging platform of a cylindrical treadmill. ISI was performed to identify the V1. On day 14, the treadmill was fixed to

minimize the motion-related artifacts, and three-dimensional (3D) z-stack images were acquired at V1 and non-V1 regions. The 512 × 512 resolution images with eight averages were acquired from 0 to 180 μm from dura in an interval of 5 μm (total 37 image stacks), in which lower 100 μm was selected for layer 2/3 analysis. The images were acquired in the same location with the same imaging parameters for longitudinal study with MD in a reference of blood vessel morphology captured by epifluorescence imaging with 605-nm LED excitation (Thorlabs). To study the effect of MD on NPTX2 secretion, the control image was acquired before the contralateral monocular eye suture, followed by imaging for three consecutive days in the same location.

NPTX2-SEP spot 3D analysis. All 3D z-stack time-series (4D) images were preprocessed with ImageJ (FIJI) and analyzed with Imaris software (Bitplane). Each set of 3D z-stack images was concatenated to generate 4D images, background corrected by "bleach correction" using a histogram-matching algorithm, and 3D drift corrected by "Correct 3D drift" algorithm (FIJI). The xyz-corrected portion of the processed 4D images was selected for NPTX2-SEP spot analysis with Imaris software. The NPTX2-SEP spots were detected with the "surface detection" function, maximum diameters of spheres detected to be 3 μm, and corresponding values within the 3D area were extracted (spot number, intensity, and volume). The "total volume" is defined by the sum of 3D compartments occupied by NPTX2-SEP–positive voxels. The spot number and the total volume were normalized with the median value of the "before" condition and presented per each animal. The mean intensity and mean volume were normalized by the median value of before condition, and all the spots from all animals were calculated. The histogram analysis was done with 5 and 25 bins for intensity and volume, respectively (Prism Graphpad).

Quantification and Statistical Analysis. Sample sizes were chosen to correspond with previous studies in which the effects of visual manipulation were measured. Animals were randomly placed into experimental groups. Whenever was possible, treatments were applied in the same animal (e.g., deprived hemisphere versus ND hemisphere) or in the same cell (e.g., electrical stimulation from layer 4 or layer 2/3; *SI Appendix*, Fig. S3*B*). For puncta quantification (Fig. 2 *C* and *D* and *SI Appendix*, Fig. S2), immunohistofluorescence quantification for NPTX2 (Fig. 3 *E* and *F*) and Western blots (*SI Appendix*, Fig. S4 *E* and *F*), the experimenter was blind to the treatment of samples during the analyses. Exclusion criteria are described for each experiment. Normality was determined using the D'Agostino test, and variance was compared using Levene's median test. Groups with normally distributed data were compared using two-tailed paired (Figs. 3*F* and 4 *E*–*G*) or unpaired *t* tests (Fig. 1 *H*, *Right* and Fig. 2*B* and *SI Appendix*, Figs. S1*N* and S6 *B* and *D*), or two-way repeated measures ANOVAs (Figs. 1*J* and 3 *C* and *D*). Sidak's post hoc tests were used for multiple comparisons following two-way ANOVAs. Groups that were not normally distributed were compared using nonparametric Wilcoxon matched pairs signed-rank test (Figs. 2*B* and 4*H* and *SI Appendix*, Figs. S3 *B* and *C* and S4), Mann–Whitney *U* test (Fig. 1 *H*, *Left* and *SI Appendix*, Fig. S1 *C*, *E*–*H*, *J*, and *M*), or ANOVAs on ranks (Fig. 4*B*; followed by Dunn's post hoc test for multiple comparisons). Statistical outliers were detected using preestablished criteria (ROUT test) and excluded from the analysis. Connectivity data were analyzed with either logistic regression test (Figs. 1 *C* and *D* and 3*G*) or a Fisher's exact test (Fig. 3 *H* and *I* and *SI Appendix*, Fig. S6 *A* and *C*). Data are presented as averages ± SEM. Statistical analyses were performed using GraphPad Software (Prism).

Data Availability. All other study data are included in the article and/or *SI Appendix*.

ACKNOWLEDGMENTS. We thank Dr. H. K. Lee and Dr. S. Zeger for valuable advice. This study was supported by NIH Grants R35 NS097966 to P.W., PO1 AG009973 to M.G., RO1NS036715 to R.L.H., R01EY016431 to E.M.Q., R01EY12124 to A.K., and R01EY025922 to E.M.Q. and A.K.

1. D. E. Feldman, Inhibition and plasticity. *Nat. Neurosci.* **3**, 303–304 (2000).
2. B. Jiang, Z. J. Huang, B. Morales, A. Kirkwood, Maturation of GABAergic transmission and the timing of plasticity in visual cortex. *Brain Res. Brain Res. Rev.* **50**, 126–133 (2005).
3. T. K. Hensch, E. M. Quinlan, Critical periods in amblyopia. *Vis. Neurosci.* **35**, E014 (2018). Correction in: *Vis. Neurosci.* **35**, E024 (2018).
4. S. J. Kuhlman *et al*., A disinhibitory microcircuit initiates critical-period plasticity in the visual cortex. *Nature* **501**, 543–546 (2013).
5. S. J. Barnes *et al*., Subnetwork-specific homeostatic plasticity in mouse visual cortex in vivo. *Neuron* **86**, 1290–1303 (2015).
6. S. H. Hendry, E. G. Jones, Reduction in number of immunostained GABAergic neurones in deprived-eye dominance columns of monkey area 17. *Nature* **320**, 750–753 (1986).
7. P. W. Hickmott, M. M. Merzenich, Local circuit properties underlying cortical reorganization. *J. Neurophysiol.* **88**, 1288–1301 (2002).
8. L. M. Levy, U. Ziemann, R. Chen, L. G. Cohen, Rapid modulation of GABA in sensorimotor cortex induced by acute deafferentation. *Ann. Neurol.* **52**, 755–761 (2002).
9. R. C. Froemke, M. M. Merzenich, C. E. Schreiner, A synaptic memory trace for cortical receptive field plasticity. *Nature* **450**, 425–429 (2007).
10. J. J. Letzkus *et al*., A disinhibitory microcircuit for associative fear learning in the auditory cortex. *Nature* **480**, 331–335 (2011).
11. Y. Gu *et al*., Obligatory role for the immediate early gene NARP in critical period plasticity. *Neuron* **79**, 335–346 (2013).
12. Y. Gu *et al*., Neuregulin-dependent regulation of fast-spiking interneuron excitability controls the timing of the critical period. *J. Neurosci.* **36**, 10285–10295 (2016).
13. Y. Sun *et al*., Neuregulin-1/ErbB4 signaling regulates visual cortical plasticity. *Neuron* **92**, 160–173 (2016).
14. J. Lu, J. Tucciarone, Y. Lin, Z. J. Huang, Input-specific maturation of synaptic dynamics of parvalbumin interneurons in primary visual cortex. *Proc. Natl. Acad. Sci. U.S.A.* **111**, 16895–16900 (2014).
15. M. E. Lambo, G. G. Turrigiano, Synaptic and intrinsic homeostatic mechanisms cooperate to increase L2/3 pyramidal neuron excitability during a late phase of critical period plasticity. *J. Neurosci.* **33**, 8810–8819 (2013).
16. X. Xu, E. M. Callaway, Laminar specificity of functional input to distinct types of inhibitory cortical neurons. *J. Neurosci.* **29**, 70–85 (2009).
17. B. Morales, S.-Y. Choi, A. Kirkwood, Dark rearing alters the development of GABAergic transmission in visual cortex. *J. Neurosci.* **22**, 8084–8090 (2002).
18. A. Goel, H.-K. Lee, Persistence of experience-induced homeostatic synaptic plasticity through adulthood in superficial layers of mouse visual cortex. *J. Neurosci.* **27**, 6692–6700 (2007).
19. C. C. Tsui *et al*., Narp, a novel member of the pentraxin family, promotes neurite outgrowth and is dynamically regulated by neuronal activity. *J. Neurosci.* **16**, 2463–2478 (1996).
20. P. Fazzari *et al*., Control of cortical GABA circuitry development by Nrg1 and ErbB4 signalling. *Nature* **464**, 1376–1380 (2010).
21. M. Martineau *et al*., Semisynthetic fluorescent pH sensors for imaging exocytosis and endocytosis. *Nat. Commun.* **8**, 1412 (2017).
22. F. Charbonnier-Beaupel *et al*., Gene expression analyses identify Narp contribution in the development of L-DOPA-induced dyskinesia. *J. Neurosci.* **35**, 96–111 (2015).
23. S. F. Cooke, M. F. Bear, How the mechanisms of long-term synaptic potentiation and depression serve experience-dependent plasticity in primary visual cortex. *Philos. Trans. R. Soc. Lond. B Biol. Sci.* **369**, 20130284 (2013). Correction in: *Philos. Trans. R. Soc. Lond. B. Biol. Sci.* **369**, 20140021 (2014).
24. K. Lehmann, S. Löwel, Age-dependent ocular dominance plasticity in adult mice. *PLoS One* **3**, e3120 (2008).
25. M. Kaneko, D. Stellwagen, R. C. Malenka, M. P. Stryker, Tumor necrosis factor-alpha mediates one component of competitive, experience-dependent plasticity in developing visual cortex. *Neuron* **58**, 673–680 (2008).
26. S. Z. Hong, S. Huang, D. Severin, A. Kirkwood, Pull-push neuromodulation of cortical plasticity enables rapid bi-directional shifts in ocular dominance. *eLife* **9**, e54455 (2020).
27. C. Chen, W. G. Regehr, Developmental remodeling of the retinogeniculate synapse. *Neuron* **28**, 955–966 (2000).
28. A. B. Patel, K. W. Loerwald, K. M. Huber, J. R. Gibson, Postsynaptic FMRP promotes the pruning of cell-to-cell connections among pyramidal neurons in the L5A neocortical network. *J. Neurosci.* **34**, 3413–3418 (2014).
29. M. Kano, T. Watanabe, Developmental synapse remodeling in the cerebellum and visual thalamus. *F1000 Res.* **8**, 10.12688/f1000research.18903.1. eCollection 2019. (2019).
30. K. P. Lamsa, D. M. Kullmann, M. A. Woodin, Spike-timing dependent plasticity in inhibitory circuits. *Front. Synaptic Neurosci.* **2**, 8 (2010).
31. S. Huang, R. L. Huganir, A. Kirkwood, Adrenergic gating of Hebbian spike-timing-dependent plasticity in cortical interneurons. *J. Neurosci.* **33**, 13171–13178 (2013).
32. H. Lee *et al*., Synapse elimination and learning rules co-regulated by MHC class I H2-Db. *Nature* **509**, 195–200 (2014).
33. M. A. Henson, C. J. Tucker, M. Zhao, S. M. Dudek, Long-term depression-associated signaling is required for an in vitro model of NMDA receptor-dependent synapse pruning. *Neurobiol. Learn. Mem.* **138**, 39–53 (2017).
34. W. C. Oh, T. C. Hill, K. Zito, Synapse-specific and size-dependent mechanisms of spine structural plasticity accompanying synaptic weakening. *Proc. Natl. Acad. Sci. U.S.A.* **110**, E305–E312 (2013).
35. J. R. Wilkerson *et al*., A role for dendritic mGluR5-mediated local translation of Arc/Arg3.1 in MEF2-dependent synapse elimination. *Cell Rep.* **7**, 1589–1600 (2014).
36. H. Maruoka *et al*., Lattice system of functionally distinct cell types in the neocortex. *Science* **358**, 610–615 (2017).
37. M. C. D. Bridi *et al*., Two distinct mechanisms for experience-dependent homeostasis. *Nat. Neurosci.* **21**, 843–850 (2018).
38. K. B. Hengen, M. E. Lambo, S. D. Van Hooser, D. B. Katz, G. G. Turrigiano, Firing rate homeostasis in visual cortex of freely behaving rodents. *Neuron* **80**, 335–342 (2013).
39. H.-K. Lee, A. Kirkwood, Mechanisms of homeostatic synaptic plasticity *in vivo*. *Front. Cell. Neurosci.* **13**, 520 (2019).
40. T. Keck, M. Hübener, T. Bonhoeffer, Interactions between synaptic homeostatic mechanisms: An attempt to reconcile BCM theory, synaptic scaling, and changing excitation/inhibition balance. *Curr. Opin. Neurobiol.* **43**, 87–93 (2017).

41. M.-F. Fong *et al*., Distinct laminar requirements for NMDA receptors in experience-dependent visual cortical plasticity. *Cereb. Cortex* **30**, 2555–2572 (2020).
42. B. Jiang, M. Treviño, A. Kirkwood, Sequential development of long-term potentiation and depression in different layers of the mouse visual cortex. *J. Neurosci.* **27**, 9648–9652 (2007).
43. M. G. Frantz *et al*., Layer 4 gates plasticity in visual cortex independent of a canonical microcircuit. *Curr. Biol.* **30**, 2962–2973.e5 (2020).
44. Z. Ma, G. G. Turrigiano, R. Wessel, K. B. Hengen, Cortical circuit dynamics are homeostatically tuned to criticality in vivo. *Neuron* **104**, 655–664.e4 (2019).
45. M. S. Bridi, S. Shin, S. Huang, A. Kirkwood, Dynamic recovery from depression enables rate encoding in inhibitory synapses. *iScience* **23**, 100940 (2020).
46. S. Huang, K. Hokenson, S. Bandyopadhyay, S. J. Russek, A. Kirkwood, Brief dark exposure reduces tonic inhibition in visual cortex. *J. Neurosci.* **35**, 15916–15920 (2015).
47. M. A. Gainey, J. W. Aman, D. E. Feldman, Rapid disinhibition by adjustment of PV intrinsic excitability during whisker map plasticity in mouse S1. *J. Neurosci.* **38**, 4749–4761 (2018).
48. Y. Guo *et al*., Dark exposure extends the integration window for spike-timing-dependent plasticity. *J. Neurosci.* **32**, 15027–15035 (2012).
49. W. Xu, S. Löwel, O. M. Schlüter, Silent synapse-based mechanisms of critical period plasticity. *Front. Cell. Neurosci.* **14**, 213 (2020).
50. M.-F. Xiao *et al*., NPTX2 and cognitive dysfunction in Alzheimer's disease. *eLife* **6**, e23798 (2017).
51. C. E. Cheetham, B. D. Grier, L. Belluscio, Bulk regional viral injection in neonatal mice enables structural and functional interrogation of defined neuronal populations throughout targeted brain areas. *Front. Neural Circuits* **9**, 72 (2015).
52. J. D. Clements, R. A. Silver, Unveiling synaptic plasticity: A new graphical and analytical approach. *Trends Neurosci.* **23**, 105–113 (2000).
53. R. Schneggenburger, E. Neher, Intracellular calcium dependence of transmitter release rates at a fast central synapse. *Nature* **406**, 889–893 (2000).
54. V. A. Kalatsky, M. P. Stryker, New paradigm for optical imaging: Temporally encoded maps of intrinsic signal. *Neuron* **38**, 529–545 (2003).